Article | Open Access

Energy Z

Xu *et al. Energy Z* **2026**, *2*, 200020 **DOI:**10.20517/energyz.2026.23

# Full concentration gradient Li-rich layered oxides cathode materials via kinetic regulation of heterogeneous nucleation growth

**Juehao Xu, Haoyan Liang, Ting Xu, Bao Qiu*, Zhaoping Liu***

**Keywords:**
Li-rich layered oxides, full concentration gradient, composition gradient, anionic redox, structural/thermal stability

**Citation:** Xu, J.; Liang, H.; Xu, T.; Qiu, B.; Liu, Z. Full concentration gradient Li-rich layered oxides cathode materials via kinetic regulation of heterogeneous nucleation growth. *Energy Z* **2026**, *2*, 200020. https://dx.doi.org/10.20517/energyz.2026.23

**Received:** 6 May 2026
**First Decision:** 8 Jun 2026
**Revised:** 2 Jul 2026
**Accepted:** 27 Aug 2026
**Published:** 11 Sep 2026

**Academic Editor:**
Xianyou Wang
**Copy Editor:**
Shu-Yuan Duan
**Production Editor:**
Shu-Yuan Duan

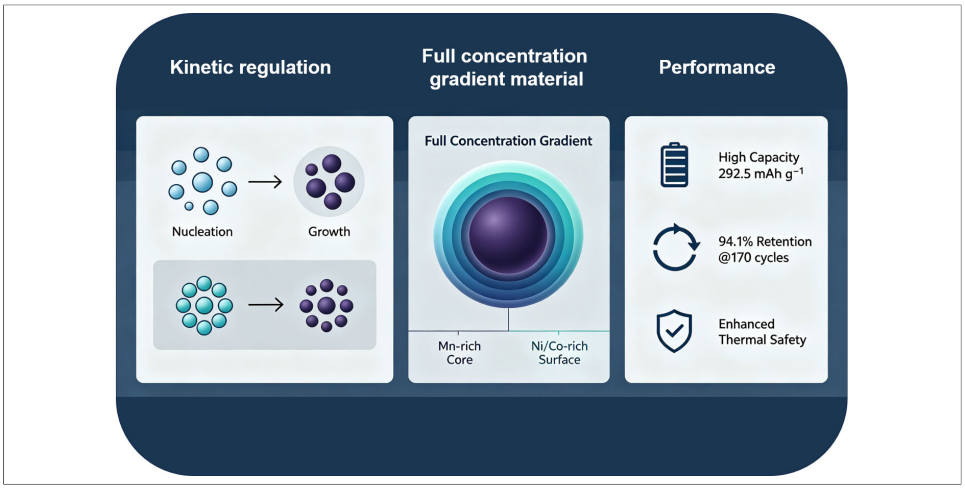


## Abstract

Li-rich layered oxides (LLOs) cathode materials deliver exceptional capacity exceeding 250 mAh $g^{-1}$ through reversible anionic redox; however, their practical application is hindered by structural instability and oxygen loss under high-voltage operation. Here, we develop a gradient partitioning strategy to construct LLOs featuring a full concentration gradient (FCG). By decoupling burst nucleation from subsequent growth, we achieve a continuous radial distribution of transition metals, resulting in a Mn-rich core and a Ni/Co-enriched surface layer. The Mn-rich core promotes bulk oxygen redox to deliver high capacity, while the Ni/Co-rich surface restricts surface oxygen redox and stabilizes the electrode-electrolyte interface. This spatial configuration decouples capacity delivery from interfacial stabilization at the single-particle scale. The optimized gradient cathode delivers an initial discharge capacity of 292.5 mAh $g^{-1}$ at 0.1 C, retains 177.8 mAh $g^{-1}$ at 5 C, and maintains 94.1% of its initial capacity after 170 cycles at 1 C. Comprehensive structural characterization, thermal analysis, and quasi-*in situ* spectroscopy confirm that the gradient design enhances both the structural and thermal stability of LLOs under high voltage conditions. By kinetically decoupling burst nucleation from growth, this strategy provides a controllable, single-step route to full concentration-gradient architectures without relying on the precise multi-pump feed-ratio programming required by conventional dual-tank



Ningbo Institute of Materials Technology & Engineering (NIMTE), Chinese Academy of Sciences, Ningbo 315201, Zhejiang, China.

*Correspondence to: Prof. Bao Qiu, Prof. Zhaoping Liu, Ningbo Institute of Materials Technology & Engineering (NIMTE), Chinese Academy of Sciences, Ningbo 315201, Zhejiang, China. E-mail: qiubao@nimte.ac.cn; liuzp@nimte.ac.cn

coprecipitation, offering a generalizable approach to stabilize anionic redox reactions in high-energy lithium-ion battery cathodes.

## INTRODUCTION

With the rapid development of high-energy-density energy storage systems, conventional intercalation-type cathodes are becoming insufficient to meet the ever-increasing demand for higher energy density[1]. Against this backdrop, Li-rich layered oxides (LLOs), which deliver discharge capacities exceeding 250 mAh $g^{-1}$, have emerged as one of the most promising candidates for next-generation high-energy-density lithium-ion battery cathodes[2]. Unlike conventional layered cathodes that rely exclusively on transition-metal cationic redox for charge compensation, LLOs exploit intrinsic Li-TM ordering in the transition-metal layers to activate reversible anionic redox, thereby breaking through the theoretical capacity ceiling of traditional intercalation cathodes[3-6].

However, under deep delithiation at high operating voltages (> 4.5 V *vs.* $Li^+/Li$), excessive anionic oxidation triggers irreversible oxygen release, which is widely recognized as the primary cause of structural and electrochemical degradation in LLOs[7-9]. The ensuing cascade involves transition-metal migration, layered-to-spinel phase transformation, oxidative electrolyte decomposition, and intergranular microcrack propagation. Collectively, these processes accelerate capacity fading and trigger exothermic reactions, compromising the thermal stability and safety of LLO cathodes[6-8,10,11]. Notably, relative to conventional intercalation-type cathodes, LLOs exhibit pronounced spatial heterogeneity in $Li^+$ (de)intercalation kinetics and anionic-redox activity[9]. Consequently, irreversible oxygen release tends to initiate at secondary-particle surfaces directly exposed to the electrolyte, posing additional challenges for maintaining structural integrity[11].

To address the structural and thermal stability challenges of LLOs, various modification strategies have been explored, including elemental doping, surface coating, and defect engineering[2,12-14]. While these approaches mitigate structural degradation and suppress detrimental interfacial side reactions - primarily by curbing $Li_2MnO_3$-activated anionic redox and reducing surface reactivity[15-17], such gains in stability often come at the expense of reversible capacity, thereby compromising the inherent high energy density advantage of LLOs[12,18]. More recently, spatial compositional regulation, particularly the full concentration gradient (FCG) design, has emerged as a promising strategy to reconcile the trade-off between capacity and stability in these materials. Core-shell architectures introduce an abrupt compositional discontinuity at the core/shell interface. This sharp boundary generates localized lattice strain and promotes microcrack initiation during cycling, driven by mismatches in lattice parameters and electrochemical activity between the two phases. The FCG design eliminates this discrete interface via a continuous radial compositional distribution, while still retaining the spatial separation of the capacity-contributing core and the stability-enhancing surface region. Given that each transition metal plays a distinct role in charge compensation: Ni primarily participates in cationic redox, Mn contributes to the C2/m phase and facilitates anionic redox, and Co engages in both cationic redox and C2/m phase formation[5,19]. The rational distribution of these elements across the secondary particle scale becomes critically important for achieving a balanced design that simultaneously delivers high capacity and robust stability. Notably, the optimal gradient trend differs between conventional NCM and LLOs. In conventional NCM, Mn or Co is typically enriched at the surface and Ni at the core to suppress the high surface reactivity of Ni-rich compositions. In LLOs, however, Mn additionally hosts the anionic-redox-active C2/m phase, making anionic redox, rather than Ni reactivity, the principal driver of surface oxygen release. An inverse gradient trend is therefore favored for LLOs, confining the Mn-rich phase to the core while enriching Ni and Co at the surface to stabilize the electrode-electrolyte interface, consistent with prior FCG designs for Li-rich cathodes.

Constructing such a gradient architecture, however, remains technically demanding. The most widely adopted route is dual-tank continuous-feeding coprecipitation, in which two precursor solutions of different transition-metal compositions are fed into the reactor at programmed, time-varying ratios to generate a continuous compositional profile. This dual-tank approach is effective in principle, but it imposes strict operational requirements. Specifically, multiple feed pumps must be precisely synchronized over the entire reaction period. Even transient fluctuations in feed ratio or supersaturation can trigger uncontrolled secondary nucleation, which degrades the uniformity and reproducibility of the final gradient profile. Additionally, nucleation and growth proceed concurrently throughout the process, making it difficult to independently tune the particle size distribution and compositional gradient steepness. These limitations motivate a synthesis strategy that separates nucleation from growth in time rather than relying solely on continuous feed-ratio programming.

In this work, we propose a kinetically controlled precision regulation strategy to construct compositionally graded Li-rich cathode materials. By applying initial high-supersaturation conditions to trigger homogeneous burst nucleation, followed by growth-controlled conditions, we achieve temporal decoupling of nucleation and growth, which enables continuous radial heterogeneous growth of the precursor and effectively suppresses secondary nucleation. This approach ultimately yields a secondary particle architecture featuring a Mn-rich core and a Ni/Co-rich outer layer. The resulting spatial elemental distribution enables synergistic optimization of capacity and cycling stability, delivering both high specific capacity (292.5 mAh $g^{-1}$ at 0.1 C) and excellent long-term cyclability (maintains 94.1% after 170 cycles at 1 C), while also mitigating the thermal degradation typically associated with high-voltage operation. From the perspectives of synthesis kinetics and spatial compositional engineering, this work demonstrates the critical role of the FCG structure in stabilizing anionic redox in LLO cathodes and provides a broadly applicable strategy for controlled synthesis and stability enhancement of high-energy-density cathode materials. This temporal decoupling reduces the dependence on continuously synchronized multi-pump feed control, thereby providing a more robust and broadly accessible route to FCG architectures.

## EXPERIMENTAL

### Materials synthesis

Synthesis of Synthesis of homogeneous Li-rich layered oxide (LR-113): $NiSO_4·6H_2O$, $CoSO_4·7H_2O$, and $MnSO_4·4H_2O$ were dissolved in stoichiometric ratios to prepare a mixed-metal solution with a total metal ion concentration of 2.0 mol $L^{-1}$. This solution, together with 2.0 mol $L^{-1}$ $Na_2CO_3$ and 0.2 mol $L^{-1}$ $NH_3·H_2O$ solutions, was continuously fed into a 5 L continuously stirred tank reactor (CSTR) using metering pumps. The coprecipitation reaction was conducted at 60 °C under a constant pH of 8.1. The resulting slurry was filtered, washed, and dried at 80 °C to obtain the $Ni_{0.2}Co_{0.2}Mn_{0.6}CO_3$ precursor. The precursor was thoroughly mixed with $Li_2CO_3$ at a Li/TM molar ratio of 1.3 and pre-calcined in air at 500 °C for 5 h, followed by calcination at 800 °C for 12 h. After natural cooling to room temperature, the final LR-113 cathode material was obtained.

Synthesis of full concentration gradient Li-rich layered oxide (LR-FCG): $NiSO_4·6H_2O$, $CoSO_4·7H_2O$, and $MnSO_4·4H_2O$ were weighed according to Ni:Co:Mn molar ratios of 1:1:4 and 1:1:1, respectively, and dissolved to prepare two mixed-metal solutions (Solution A and Solution B) with a total metal ion concentration of 2.0 mol $L^{-1}$. Under continuous stirring, Solution B was gradually introduced into Solution A to form a preliminary compositional gradient. The mixed-metal solution, together with 2.0 mol $L^{-1}$ $Na_2CO_3$ and 0.2 mol $L^{-1}$ $NH_3·H_2O$ solutions, was continuously fed into a 5 L CSTR using metering pumps. Coprecipitation was performed at 60 °C under a constant pH of 8.1. The obtained slurry was filtered, washed, and dried at 80 °C to yield a $Ni_{0.2}Co_{0.2}Mn_{0.6}CO_3$ precursor with a compositional gradient. The precursor was then thoroughly mixed with $Li_2CO_3$ at a Li/TM molar ratio of 1.3 and pre-calcined in air at 500 °C for 5 h,

followed by calcination at 800 °C for 12 h. After natural cooling, the final LR-FCG cathode material was obtained.

## Electrochemical measurements

CR2032-type coin cells were assembled in an argon-filled glove box ($H_2O$ and $O_2$ < 0.1 ppm). Cathode electrodes were prepared by mixing active material, Super P conductive carbon, and polyvinylidene fluoride (PVDF) binder at an 80:10:10 mass ratio and coating them onto a current collector to an areal loading of ~5 mg $cm^{-2}$. Lithium metal served as the counter electrode, Celgard 2502 as the separator, and 1.0 M $LiPF_6$ in ethylene carbonate/dimethyl carbonate (3: 7 V/V) as the electrolyte. All measurements were conducted at 25 °C. Galvanostatic charge-discharge tests were performed on a LAND-CT2100A battery tester at a specific current corresponding to 250 mA $g^{-1}$. Kinetic properties were evaluated via the galvanostatic intermittent titration technique (GITT) using 0.05 C current pulses for 30 min, followed by 2 h relaxation.

## Characterization

X-ray diffraction (XRD) patterns were recorded on a D8 DISCOVER diffractometer (Bruker). Particle morphology was examined using a S-4800 scanning electron microscope (Hitachi), and particle size distributions were measured with a HELOS-OASIS laser diffraction system (Sympatec). Cross-sections of secondary particles were prepared using a dual-beam focused ion beam-scanning electron microscope (FIB-SEM, Auriga, Carl Zeiss) combined with ion polishing, and the elemental distributions of Ni, Co, and Mn were analyzed using the attached energy-dispersive X-ray spectroscopy (EDS) system. The overall chemical compositions of the samples were determined by inductively coupled plasma optical emission spectroscopy (ICP-OES, SPECTRO ARCOS).

DSC Measurements: Differential scanning calorimetry (DSC) was performed using a DSC 6000 (Perkin Elmer) under flowing high-purity nitrogen. Samples were heated from 25 °C to 350 °C at 10 °C $min^{-1}$. Charged cathode powders were obtained by disassembling first-cycle coin cells inside a glove box, rinsing electrodes with dimethyl carbonate (DMC), drying, and scraping the cathode powder (including binder and conductive carbon) into a stainless steel high-pressure crucible. Electrolyte was added at a mass ratio of 1:1 (cathode material:electrolyte) before DSC testing.

TG-MS Measurements: Thermogravimetry coupled with mass spectrometry (TG-MS) was performed using a TGA8000 combined with a Clarus SQ8T mass spectrometer (Perkin Elmer) under high-purity flowing argon. Cathode powders were obtained by disassembling CR2032 cells, rinsing with DMC, and scraping from the current collector in an argon glove box. After sealing, samples were transferred to alumina crucibles and heated from 50 °C to 600 °C at 10 °C $min^{-1}$.

*In situ* Heating Raman Spectroscopy: *In situ* Raman measurements were conducted using a LabRAM Odyssey spectrometer (Horiba) with a 532 nm laser. Cathode powders were prepared as above and transferred into alumina crucibles placed in a custom *in situ* heating chamber. Measurements were performed from 20 °C to 400 °C at 10 °C $min^{-1}$, with a 5 min stabilization at each 20 °C increment prior to spectral acquisition.

Hard X-ray Absorption Spectroscopy (XAS): Transmission-mode XAS measurements were carried out at the BL13SSW beamline of the Shanghai Synchrotron Radiation Facility (SSRF). Standard reference samples (Ni, Co, and Mn foils) were measured simultaneously. X-ray absorption near-edge structure (XANES) and extended X-ray absorption fine structure (EXAFS) data were processed and fitted using the ATHENA software package[20].

## RESULTS AND DISCUSSION

### Synthesis strategy and mechanism

In coprecipitation systems, supersaturation provides the thermodynamic driving force for phase transformation and is defined as:

$$S = \frac{C}{C_{eq}} \tag{1}$$

where $C$ is the effective solute concentration in the solution, and $C_{eq}$ is the equilibrium solubility[21]. The corresponding chemical-potential driving force can be expressed as:

$$\Delta\mu = k_B T \ln S = k_B T \ln \frac{C}{C_{eq}} \tag{2}$$

where $k_B$ is the Boltzmann constant, and $T$ is the absolute temperature. According to classical nucleation theory, the critical nucleation free-energy barrier $\Delta G^*$ exhibits a nonlinear dependence on $ln\ S$[22]:

$$\Delta G^* \propto \frac{1}{(\ln S)^2} \tag{3}$$

Consequently, the nucleation rate is exponentially sensitive to supersaturation[22,23]:

$$J \propto e^{\left(-\frac{\Delta G^*}{k_B T}\right)} \tag{4}$$

Therefore, increasing the solute concentration $C$ at the early stage of the reaction increases $\Delta\mu$, thereby lowering the nucleation barrier and accelerating the overall reaction kinetics[22]. In coprecipitation reactions, the nucleation barriers for homogeneous and heterogeneous nucleation generally satisfy:

$$\Delta G^*_{\text{het}} = f \Delta G^*_{\text{hom}} \tag{5}$$

where $0 < f < 1$, $\Delta G_{hom}{}^*$ denotes the homogeneous nucleation barrier, and $\Delta G_{het}{}^*$ denotes the heterogeneous nucleation barrier. This relationship indicates that heterogeneous nucleation proceeds with a lower free-energy barrier than homogeneous nucleation[24,25]. As shown in Supplementary Figures 1 and 2, during crystallization the solute concentration first exceeds the equilibrium concentration $C_{eq}$, leading to the formation of unstable clusters in solution. When the concentration further increases to the minimum nucleation concentration $C_{nuc}$, stable nuclei are generated via homogeneous nucleation[23]. As solute is rapidly consumed, the concentration decreases to below $C_{nuc}$ while remaining above $C_{eq}$ ($C_{eq} < C < C_{nuc}$). Since the concentration no longer reaches $C_{nuc}$, the thermodynamic barrier for homogeneous nucleation cannot be overcome, and the system enters a growth stage dominated by heterogeneous deposition on the preformed nuclei[21].

As illustrated in Figure 1, a high-supersaturation protocol was applied at the initial stage to generate a large number of nuclei, thereby providing abundant and uniformly distributed growth sites for the subsequent deposition and particle growth. As the reaction proceeds, solute consumption and replenishment gradually reach a dynamic balance. The solute concentration thus decreases further and approaches a quasi-steady state, falling below $C_{nuc}$ and entering the growth window ($C_{eq} < C < C_{nuc}$). This transition marks a shift from a nucleation-dominated regime to a growth-dominated regime. It produces a stable, uniformly distributed population of nuclei, providing a controllable foundation for subsequent continuous radial gradient growth.

As shown in Supplementary Figure 1, the gradient synthesis is carried out within the growth window ($C_{eq} < C < C_{nuc}$). Using the designed reactor setup, the transition-metal concentration in the solution flowing through

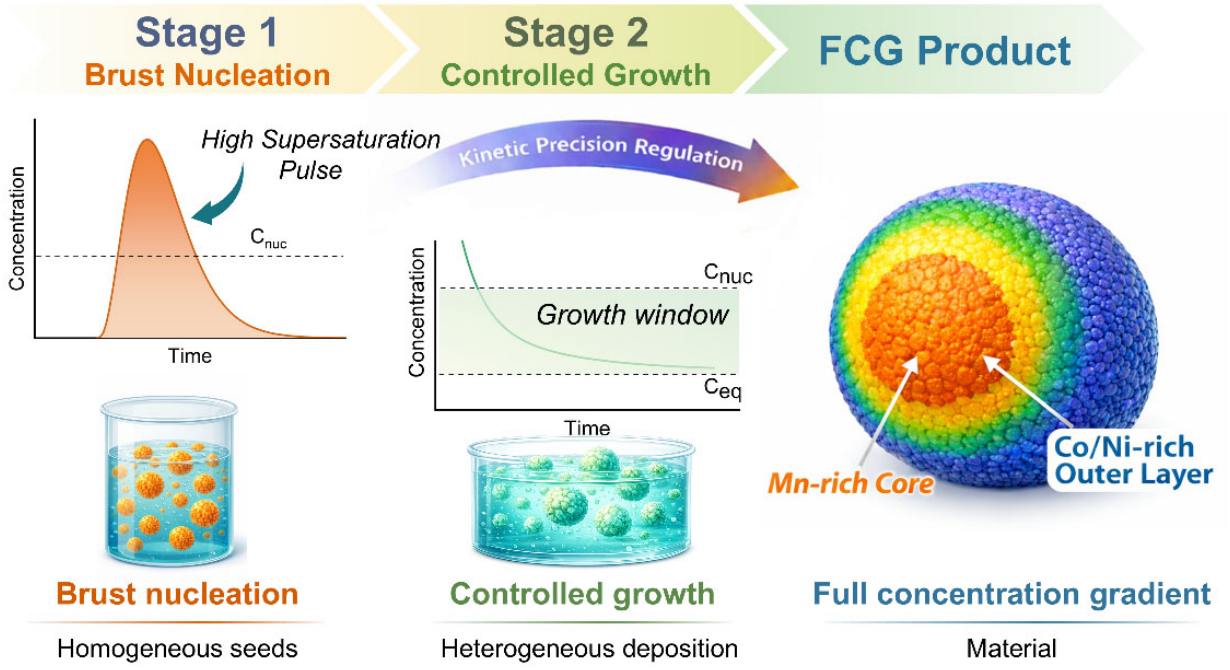


**Figure 1.** Schematic illustration of the kinetic control strategy for synthesizing FCG precursors. An initially high solute concentration is deliberately provided to drive a burst of homogeneous nucleation, generating abundant nuclei that serve as seeds for subsequent particle growth. As the reaction proceeds, the supersaturation gradually decreases, and the process becomes growth-dominated (heterogeneous deposition on existing nuclei) rather than further nucleation. Meanwhile, the time-programmed evolution of transition-metal (TM) concentrations in the solution continuously modulates the deposited composition, ultimately producing a radially continuous full concentration gradient within individual precursor particles. $C_{nuc}$: Nucleation concentration; $C_{eq}$: equilibrium concentration; FCG: full concentration gradient.

the reactor is programmed to follow a predefined time-dependent profile. This time-dependent profile is then translated into radial particle growth, enabling the formation of the concentration-gradient cathode material.

The time-dependent evolution of precursor morphology and composition further corroborates the effectiveness of the strategy. Scanning electron microscopy (SEM) images reveal progressive particle densification, showing a transition from loosely aggregated primary nuclei at the early stage to dense secondary particles with smooth surfaces and high sphericity [Figure 2A]. Particle size distribution (PSD) analysis shows that D50 increases linearly and monotonically with reaction time [Figure 2B and Supplementary Figure 3], while the distribution remains consistently narrow, indicating that growth is dominated by heterogeneous deposition and secondary nucleation is suppressed. More importantly, EDS analysis of particle surfaces collected at different reaction times [Figure 2C and Supplementary Figure 4] shows that the metal molar ratios (Ni:Co:Mn) closely match the corresponding instantaneous feed compositions delivered to the reactor. This close match between liquid-phase feed composition and solid-phase surface composition confirms that precipitation occurs primarily on the surfaces of growing particles, enabling the formation of a continuous FCG architecture.

## Structural and morphological characterization

To systematically evaluate the effect of a full concentration gradient design on the structure and performance of LLO cathodes, two samples with similar overall chemical compositions but distinct spatial compositional distributions were prepared. The cathode with a radial concentration gradient, synthesized via the gradient-regulation strategy, is designated as LR-FCG. In contrast, a reference sample with the same average

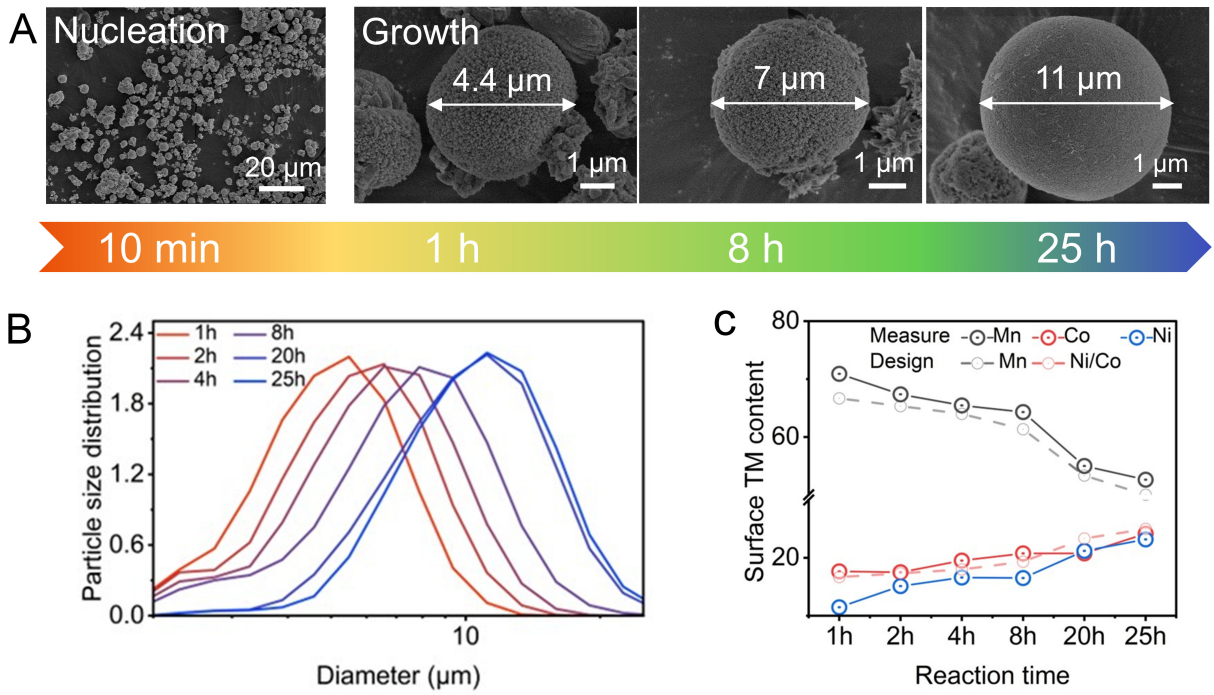


**Figure 2.** Synthesis monitoring of the full-concentration-gradient cathode material. (A) SEM images of precursor particles collected at different reaction times during the synthesis process; (B) Particle size distributions of the precursors at different synthesis stages; (C) Surface elemental compositions of precursor particles collected at different reaction times, obtained from EDS analysis. SEM: Scanning electron microscopy; EDS: energy-dispersive X-ray spectroscopy.

composition as LR-FCG but lacking a radial compositional gradient, in which transition metals are uniformly distributed throughout the particles, is denoted as LR-113. Similar overall chemical compositions were confirmed by inductively coupled plasma optical emission spectroscopy (ICP-OES) [Supplementary Table 1]. The overall morphology and particle configuration were examined by SEM. As shown in Supplementary Figure 5, both LR-113 and LR-FCG display regular spherical secondary particles with similar size distributions, each composed of densely packed submicron primary particles. The specific surface area and pore-structure analyses are summarized in Supplementary Figure 6. Compared with LR-113, LR-FCG exhibits a more open internal structure, as reflected by an increase in specific surface area from 6.09 to 7.09 $m^2 g^{-1}$ and an increase in average pore diameter from 19.61 to 19.94 nm. This more developed porosity enhances electrolyte wetting and provides smoother pathways for subsequent $Li^+$ transport[26].

EDS was initially used to directly probe the radial elemental distribution in the particles. Line-scan analyses across cross-sections of both the precursors and the sintered cathode particles enabled tracking of gradient formation and retention during synthesis. As shown in Supplementary Figure 7, the compositionally uniform precursor P-113 displayed a homogeneous distribution of all transition-metal elements along the particle radius. In contrast, the precursor P-FCG already exhibited a distinct radial concentration gradient, indicating that the designed full concentration gradient had been successfully established in the precursor. After high-temperature solid-state lithiation and sintering, the elemental distribution remained intact. For the homogeneous sample LR-113, its cross-sectional SEM image is shown in Figure 3A, and the corresponding cross-sectional EDS line-scan profiles are presented in Figure 3B, confirming uniform distribution of all transition-metal elements. The powder XRD pattern of LR-113 analyzed by Rietveld refinement is shown in Figure 3C.

For the gradient sample LR-FCG, Figure 3D shows its cross-sectional SEM morphology, and Figure 3E presents the corresponding EDS line-scan profiles, confirming that the radial concentration gradient was

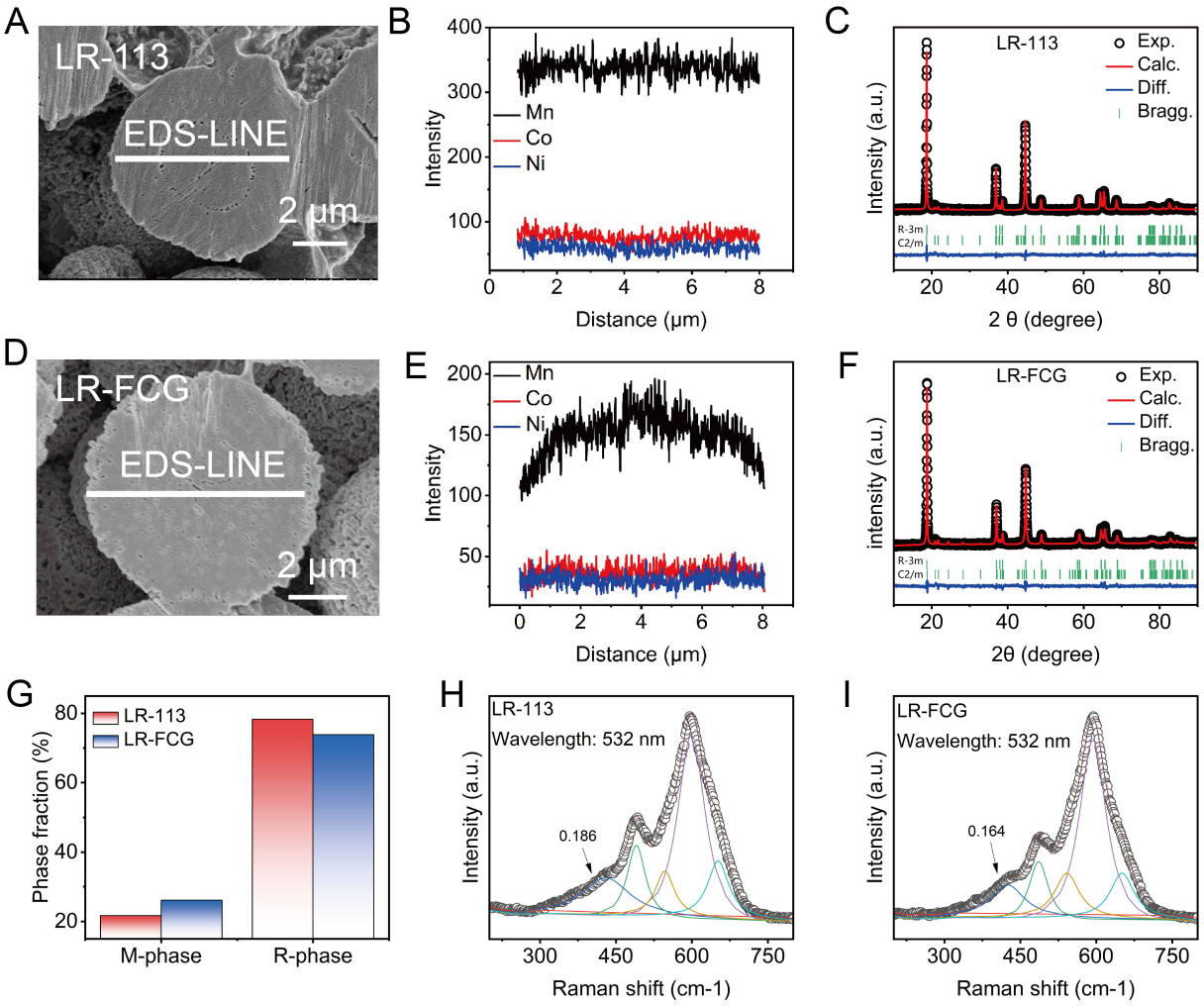


**Figure 3.** Morphology and structural characterization of LR-113 and LR-FCG. (A) Cross-sectional SEM image of LR-113; (B) Cross-sectional EDS line-scan profiles of LR-113; (C) Rietveld-refined XRD pattern of LR-113; (D) Cross-sectional SEM image of LR-FCG; (E) Cross-sectional EDS line-scan profiles of LR-FCG; (F) Rietveld-refined XRD pattern of LR-FCG; (G) Comparison of phase fractions for LR-113 and LR-FCG obtained from Rietveld refinement; (H) Raman spectrum of LR-113 collected with an excitation wavelength of 532 nm; (I) Raman spectrum of LR-FCG collected with an excitation wavelength of 532 nm. LR-FCG: Li-rich layered oxide; EDS: energy-dispersive X-ray spectroscopy; SEM: scanning electron microscopy; XRD: X-ray diffraction.

well preserved after sintering. Transmission electron microscopy and corresponding EDS mapping [Supplementary Figure 8] further corroborate that transition-metal elements are uniformly distributed within individual primary particles, indicating that the gradient primarily exists at the secondary-particle scale rather than arising from inhomogeneity within primary particles. The Rietveld-refined XRD pattern of LR-FCG is shown in Figure 3F. The overall XRD patterns of LR-113 and LR-FCG are shown in Supplementary Figure 9.

The refinement results indicate that both samples consist of a hexagonal layered α-$NaFeO_2$ phase (space group R-3m) and a monoclinic $Li_2MnO_3$ phase (space group C2/m)[26]. The comparison of phase fractions for LR-113 and LR-FCG obtained from Rietveld refinement is shown in Figure 3G. Notably, compared with LR-113, LR-FCG exhibits a higher refined $Li_2MnO_3$ phase fraction, which is consistent with its Mn-rich core region. The refined lattice parameters a and c of LR-FCG show slight contraction, resulting in a modest reduction in unit-cell volume, which is consistent with its higher $Li_2MnO_3$ fraction[27]. Additionally, the refinement results reveal an increased Li-O layer thickness in LR-FCG [Supplementary Table 2], which

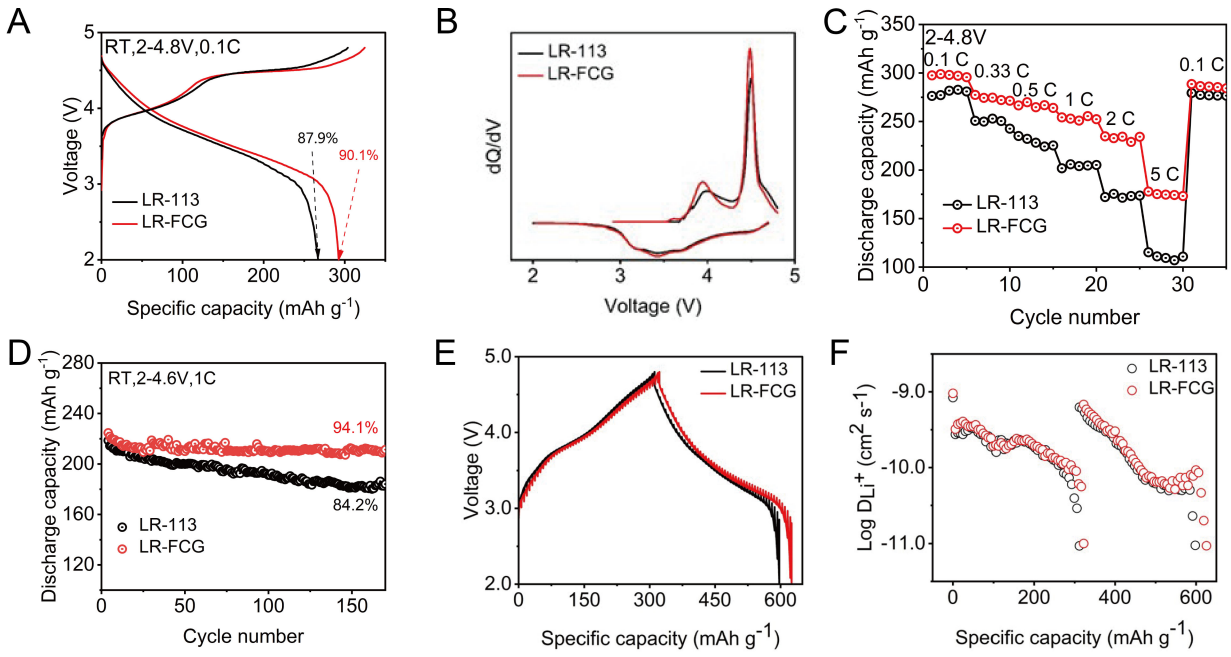


**Figure 4.** Electrochemical performance and kinetic analysis of the LR-FCG and LR-113 cathodes in half-cells. (A) Comparison of the initial charge-discharge curves at room temperature (RT) within 2.0-4.8 V at 0.1 C (1 C = 250 mA $g^{-1}$); (B) The corresponding differential capacity (dQ/dV) curves; (C) Rate capability at various current densities; (D) Cycling performance at 1 C within the voltage window of 2.0-4.6 V at RT; (E) GITT curves obtained during the second cycle; (F) Comparison of the calculated $Li^+$ diffusion coefficients ($D_{Li^+}$) during the charge and discharge processes. LR-FCG: Li-rich layered oxide; GITT: galvanostatic intermittent titration technique.

effectively widens the two-dimensional $Li^+$ diffusion pathways and may contribute to improved rate capability under high-rate conditions[28].

Raman spectroscopy under different excitation conditions was employed to probe the near-surface structure of the particles. As shown in Figure 3H and I, and Supplementary Figure 10, under 532 nm excitation (shallower penetration depth), LR-FCG exhibits a weaker $Li_2MnO_3$-related band at ~ 425 $cm^{-1}$ than LR-113[29]. Peak fitting quantitatively confirms this trend and indicates Ni/Co enrichment and Mn depletion in the surface region of LR-FCG. This near-surface composition with lower $Li_2MnO_3$ content is expected to enhance electronic transport and mitigate lattice-oxygen release at high voltages. In contrast, under 785 nm excitation (deeper penetration into the bulk), both samples show comparable $Li_2MnO_3$ signals, consistent with a Mn-rich core. The distinct spectral responses between 532 and 785 nm excitations support that the full concentration-gradient design achieves the intended functional zoning between the near-surface region and the particle interior.

## Electrochemical performance

As shown in Figure 4A, during the initial charge-discharge at 0.1 C (1 C = 250 mA $g^{-1}$), LR-FCG delivers an initial discharge capacity of 292.5 mAh $g^{-1}$, corresponding to a 9.5% increase relative to LR-113 (267.1 mAh $g^{-1}$). Differential capacity plots [Figure 4B] further show that LR-FCG exhibits a larger capacity contribution in the high-voltage region, consistent with enhanced anionic (oxygen) redox activity. LR-FCG achieves an initial Coulombic efficiency of 90.1%, exceeding that of LR-113 (87.9%). The improved electrochemical performance may be attributed to associated with the Mn-rich region in the gradient structure, which promotes high-voltage oxygen redox activity and thus contributes to the increased charge and discharge capacities during the initial cycle[30].

The regulatory effect of the gradient architecture on internal reaction kinetics is further reflected in the rate capability and cycling performance. As shown in Figure 4C, during rate capability tests conducted over 2.0-4.8 V, LR-FCG delivers 177.8 mAh $g^{-1}$ even at 5C, significantly higher than LR-113 (115.3 mAh $g^{-1}$). This result indicates an improved kinetic response of LR-FCG during high-rate charge-discharge cycling. In long-term cycling at 1 C over 2.0-4.6 V [Figure 4D], LR-FCG retains 94.1% of its initial capacity after 170 cycles, corresponding to a reversible capacity of 211.4 mAh $g^{-1}$. By contrast, LR-113 shows lower capacity retention (84.2%), with a remaining capacity of 184.1 mAh $g^{-1}$. Collectively, these results demonstrate that the gradient structure enables superior rate performance and improved long-term cycling stability under moderate cutoff voltages.

The $Li^+$ diffusion kinetics of both samples were further evaluated using the galvanostatic intermittent titration technique (GITT). During first-cycle electrochemical activation, both samples exhibit comparable $Li^+$ diffusion coefficients [Supplementary Figure 11]. This may be mainly attributed to the increased $Li_2MnO_3$-related content in LR-FCG, because a higher $Li_2MnO_3$ fraction can reduce the electronic conductivity of the material and thus limit $Li^+$ transport during the initial activation process. Notably, after first-cycle activation, second-cycle GITT measurements [Figure 4E and F] show that LR-FCG exhibits apparently higher $Li^+$ diffusion coefficients than LR-113, indicating that the gradient architecture promotes ion-transport kinetics after electrochemical activation.

In summary, compared with the homogeneous LR-113, gradient-designed LR-FCG demonstrates advantages in reversible capacity, rate performance, cycling stability, and $Li^+$ transport kinetics. These results collectively demonstrate that constructing a compositional gradient to regulate reaction heterogeneity is a promising strategy for enhancing the overall performance of Li-rich Mn-based cathodes.

## Structural and thermal stability

To elucidate the structural origin of cycling stability, Raman spectroscopy was conducted on the electrodes after 170 cycles at 1C between 2.0 and 4.6 V. As shown in Supplementary Figure 12, the characteristic band at ~ 600-650 $cm^{-1}$ (ca. 625 $cm^{-1}$) can be assigned to the $A_{1g}$ symmetric stretching vibration of Mn-O bonds in a spinel phase (space group Fd-3m)[31]. This band is commonly regarded as an indicator of spinel-like surface reconstruction in layered cathodes. Compared with LR-FCG, LR-113 shows higher intensity in this region, indicating that its particle surface is more susceptible to irreversible reconstruction from the layered structure toward a spinel-like phase during cycling. In contrast, the weakened intensity of LR-FCG suggests that the Ni/Co-enriched surface gradient layer helps stabilize the surface lattice and suppress electrolyte-attack-induced surface reconstruction and phase transition, thereby providing structural evidence for its improved cycling stability[32-34].

Supplementary Figure 13A-C shows *ex situ* XRD patterns of the cycled electrodes. After cycling, both materials largely retain the main diffraction features of the α-$NaFeO_2$-type layered structure, indicating that the layered framework is generally preserved. However, clear differences are observed in the evolution of the diffraction peaks. Compared with LR-FCG, LR-113 shows a more obvious decrease in peak intensity and a more pronounced peak broadening for the characteristic reflections after cycling, suggesting more severe structural degradation and a higher degree of structural disorder. In contrast, LR-FCG maintains relatively stronger and sharper diffraction peaks, implying that the gradient architecture helps preserve the layered structure during prolonged cycling. These results further support the improved structural stability of LR-FCG[35].

To evaluate the thermal stability of the cathode materials at a high state of charge, differential scanning calorimetry (DSC) was performed on cathode samples charged to 4.8 V (*vs.* $Li^+$/Li). To better approximate practical cell conditions, the charged cathode powders were directly mixed with an organic electrolyte at a

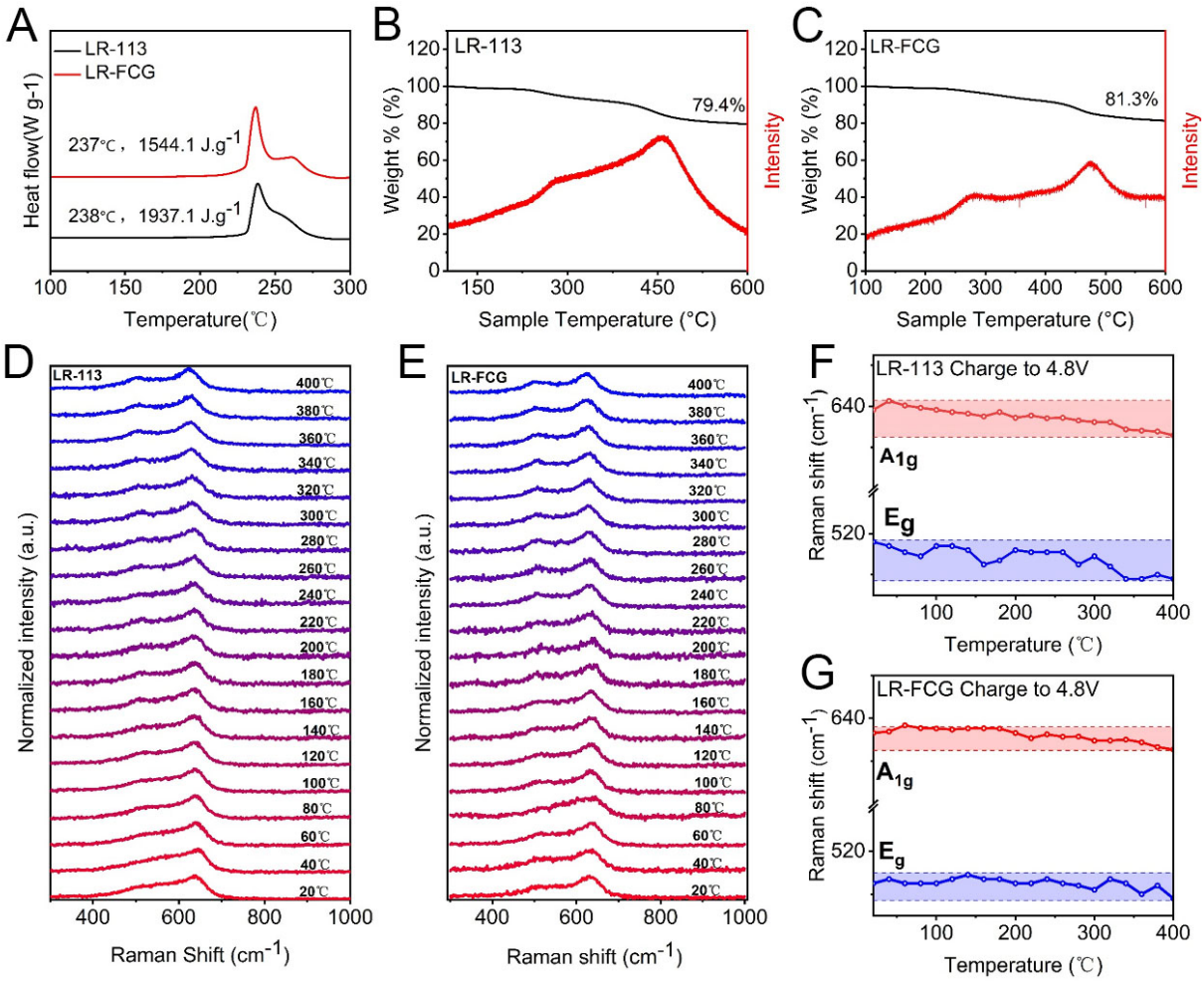


**Figure 5.** Thermal stability of fully charged LR-113 and LR-FCG cathodes. (A) Differential scanning calorimetry (DSC) curves of fully charged LR-113 and LR-FCG cathodes mixed with electrolyte at a weight ratio of 1:1; (B and C) Thermogravimetric (TG) curves of fully charged LR-113 and LR-FCG cathodes, respectively, with simultaneous mass spectrometry (MS) monitoring of oxygen release during heating; (D and E) In situ Raman spectra of fully charged LR-113 and LR-FCG cathodes collected at elevated temperatures; (F and G) Temperature-dependent evolution of characteristic Raman peak positions for LR-113 and LR-FCG during heating. LR-FCG: Li-rich layered oxide.

1:1 mass ratio prior to testing. The main exothermic peak in DSC profiles arises from multiple heat-releasing processes, including lattice-oxygen release from highly charged cathodes and accompanying oxidative electrolyte decomposition. This peak is therefore widely used as an indicator of thermal runaway risk[12,36,37]. As shown in Figure 5A, LR-113 and LR-FCG exhibit comparable onset temperatures for heat release (ca. 237-238 °C), suggesting a similar temperature threshold for triggering thermal events; however, their total heat release shows a clear difference. LR-113 releases 1,937.1 J $g^{-1}$, whereas LR-FCG releases 1,544.1 J $g^{-1}$. This reduction in heat release indicates that LR-FCG has better thermal stability.

Lattice-oxygen release is widely considered a key origin of thermal instability in highly delithiated layered cathodes[38]. To further elucidate the mass-loss behavior and gas evolution associated with oxygen liberation during heating, thermogravimetry coupled with mass spectrometry (TG-MS) was employed for operando monitoring [Figure 5B and C]. The TG results reveal a total weight loss of 20.6% for LR-113, which is reduced to 18.7% for LR-FCG, indicating that thermally induced mass loss is mitigated to some extent in the gradient sample. In conjunction with the DTG curves [Supplementary Figure 14], the temperature of the maximum weight-loss rate closely coincides with the $O_2$ signal (m/z = 32) detected by MS, indicating that the

dominant mass-loss event is strongly coupled with oxygen release and that lattice-oxygen evolution is predominant in this high-temperature region. Notably, LR-113 shows a sharper, more intense $O_2$ peak, indicating more concentrated oxygen release within a narrower temperature interval. By contrast, LR-FCG shows a weakened and broadened $O_2$ signal, suggesting moderated and delayed oxygen evolution. These observations indicate that the dense Ni/Co-rich gradient layer in LR-FCG enhances the stability of surface TM-O bonds and lowers the propensity for oxygen release, consistent with the suppressed exothermic behavior observed in DSC.

To further uncover the atomic-scale origin of the thermal-stability disparity, temperature-dependent *operando* Raman spectroscopy was conducted to track the evolution of lattice vibrations during heating. As shown in Figure 5D-G, with increasing temperature, the $A_{1g}$ mode, associated with symmetric TM-O stretching along the c axis, exhibits a red shift in both samples, but the shift is substantially larger for LR-113 than for LR-FCG. Typically, a larger red shift reflects more substantial TM-O bond softening and a stronger thermal structural response, consistent with the stronger $O_2$ evolution inferred from TG-MS. In contrast, the smaller red shift for LR-FCG suggests a more robust lattice upon heating, which may help mitigate oxygen activation and release at high temperature. Further analysis of the $E_g$ mode, which is related to in-plane vibrations within the ab plane, shows an overall red shift with increasing temperature accompanied by non-monotonic fluctuations. Such transient upshifts are commonly associated with local spinel-like transformation and/or structural reconstruction driven by transition-metal migration. The fluctuation is more pronounced for LR-113, implying more extensive cation migration and lattice rearrangement during heating[39-42]. By comparison, the attenuated oscillation in LR-FCG indicates that the outer Ni/Co-enriched gradient shell suppresses cation migration and the associated phase-transition processes. Collectively, the full concentration-gradient design of LR-FCG synergistically modulates high-temperature structural evolution by chemically lowering oxygen reactivity and structurally inhibiting cation rearrangement.

## Local structure and evolution mechanism analysis

To further elucidate the influence of the concentration-gradient architecture on high-voltage reaction reversibility and local structural stability in Li-rich cathodes, X-ray absorption spectroscopy (XAS) was performed on samples harvested at selected electrochemical states. XANES tracked the evolution and reversibility of average transition-metal oxidation states, whereas Fourier-transformed EXAFS (FT-EXAFS) and quantitative fitting probed the structural response of the TM-O coordination shell and the associated accumulation and recovery of local disorder.

As shown in the Mn K-edge XANES spectra [Figure 6A], charging to 4.8 V results in a slight shift of the absorption edge to lower energy rather than a further positive shift. This behavior indicates that conventional Mn cationic oxidation is not dominant in the high-voltage region; instead, it likely involves activation of anionic redox and rearrangement of the local Mn-O environment. After discharging to 2.0 V, the Mn absorption edge of LR-113 fails to fully return to its initial position, suggesting partial irreversibility in Mn-related valence evolution and accompanying local structural changes[43]. By contrast, LR-FCG shows clearer edge recovery, indicating better reversibility of Mn-associated redox/structural evolution. This difference is consistent with the design rationale that the gradient architecture confines the Mn-rich region toward the particle interior, thereby reducing its interfacial reactivity and susceptibility to degradation under high-voltage operation. Co K-edge XANES spectra [Figure 6B] show that Co undergoes reversible oxidation upon charging in both materials. However, after discharge, the absorption edge of LR-113 shifts slightly to lower energy relative to the initial state, implying partial irreversibility in the local Co-O coordination environment. In comparison, the Co edge of LR-FCG almost fully returns to the initial position, suggesting a more stable Co local environment. For the Ni K-edge XANES spectra [Figure 6C], the edge evolution in the two materials is highly consistent and largely reversible, indicating that Ni, as the primary cationic redox

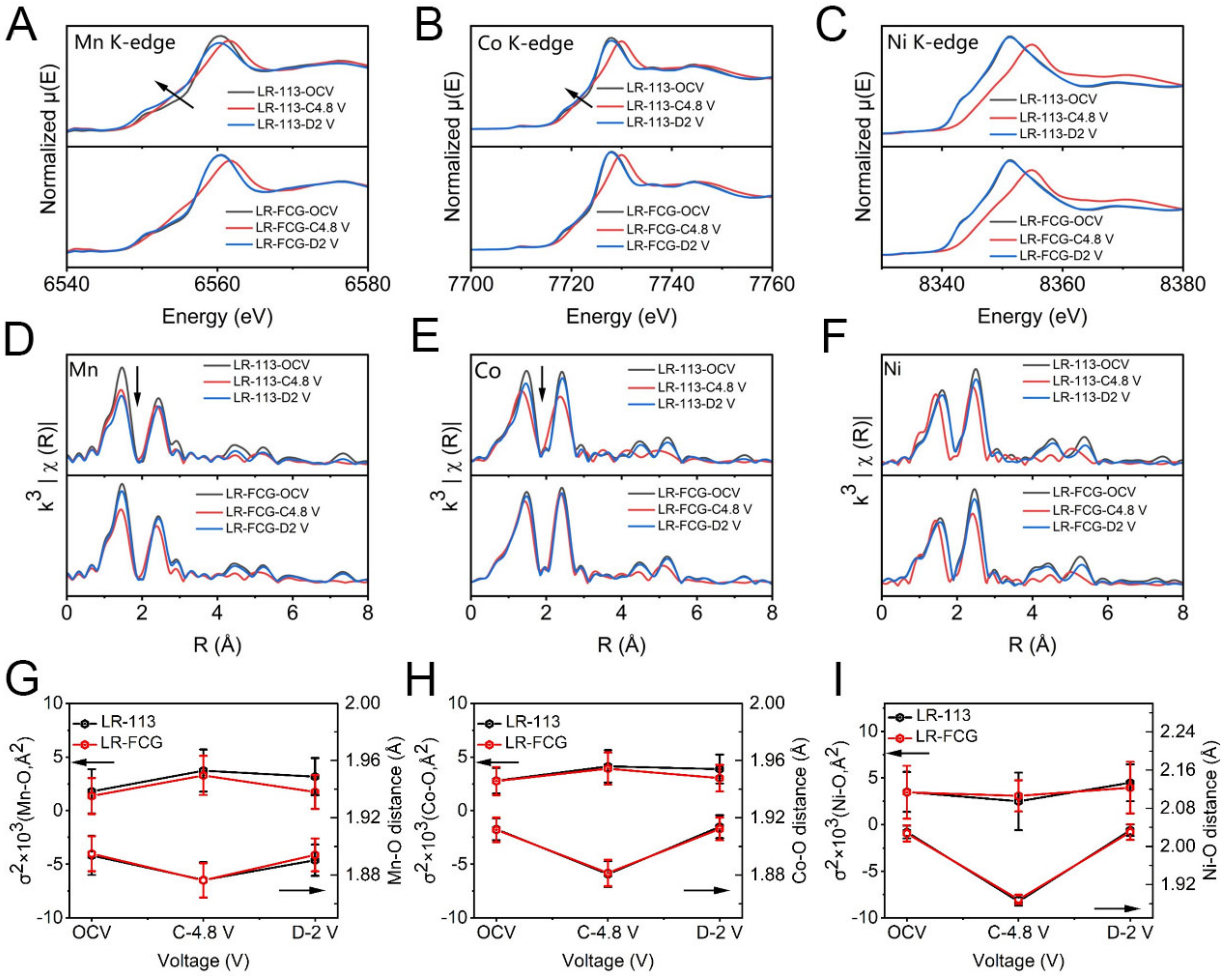


**Figure 6.** Local structural evolution of LR-113 and LR-FCG during electrochemical cycling. (A-C) X-ray absorption near-edge structure (XANES) spectra at the Mn, Co, and Ni K-edges of LR-113 and LR-FCG at the open-circuit voltage (OCV), fully charged state (C-4.8 V), and discharged state (d-2.0 V); (D-F) Fourier-transformed (FT) Mn, Co, and Ni K-edge EXAFS spectra of LR-113 and LR-FCG at OCV, fully charged, and discharged states; (G-I) Fitted bond distances and Debye-Waller factors of Mn-O, Co-O, and Ni-O coordination shells for LR-113 and LR-FCG at different electrochemical states. The error bars represent the fitting uncertainty (estimated standard deviation) of the EXAFS refinement. LR-FCG: Li-rich layered oxide; EXAFS: extended X-ray absorption fine structure.

center, undergoes intrinsic valence evolution that is only weakly affected by the gradient design[19].

FT-EXAFS further reveals local structural differences associated with the valence evolution discussed above [Figure 6D-F]. For the Mn K-edge, LR-113 shows pronounced attenuation of the Mn-O first-shell peak in the charged state and incomplete recovery upon discharge, indicating enhanced local coordination disorder. In contrast, LR-FCG shows a more evident rebound of the first-shell peak upon discharge, indicating improved local-structural recoverability. A similar trend is observed at the Co K-edge: LR-113 exhibits greater attenuation of the Co-O coordination peak at high voltage and poorer recovery, whereas LR-FCG shows a smaller variation. The fitting results [Figure 6G-I and Supplementary Figure 15] further show that LR-113 undergoes a larger increase in the Debye-Waller factor across electrochemical states, implying a greater tendency for local disorder to accumulate. By comparison, LR-FCG exhibits more constrained disorder evolution and more complete recovery[44].

Overall, the Ni/Co-enriched surface gradient layer tends to accommodate reversible cationic redox and spatially buffer the high-voltage activity of the Mn-rich core, which may help reduce the risk of irreversible local reconstruction. This conclusion is consistent with the stabilization trends revealed by the

aforementioned thermal analysis and oxygen-evolution characterizations.

## CONCLUSIONS

In summary, we develop a kinetic-precision control strategy that temporally decouples nucleation from growth, enabling the construction of Li-rich Mn-based cathodes with a FCG architecture. The continuous radial distribution of transition metals spatially separates bulk anionic redox activity from surface stabilization, eliminating abrupt compositional interfaces. Notably, this Mn-rich core/Ni-Co-rich surface arrangement is inverse to the gradient trend typically adopted in conventional NCM cathodes, reflecting the distinct role of Mn as the host of anionic-redox activity in Li-rich systems. The Mn-rich core delivers high reversible capacity through bulk anionic redox, whereas the Ni/Co-enriched surface gradient strengthens the TM-O framework, mitigating lattice-oxygen release and surface reconstruction and reducing the tendency for transition-metal migration at high voltage, thereby improving rate capability and cycling stability. Thermal analyses further reveal reduced and delayed oxygen evolution, which mitigates exothermic cathode-electrolyte reactions and improves thermal safety. Quasi-*in situ* XAS confirms more reversible Mn/Co valence evolution and TM-O coordination with limited disorder accumulation during cycling. These results demonstrate that compositional-gradient engineering enabled by kinetic precision control offers an effective and generalizable route to simultaneously advance performance and safety in high-energy-density Li-ion cathodes.

## DECLARATIONS

### Authors' contributions

Conceptualization: Xu, J; Qiu, B; Liu, Z.
Investigation and visualization: Xu, J; Qiu, B.
Methodology and formal analysis: Xu, J; Xu, T; Qiu, B; Liu, Z.
Writing - original draft: Xu, J.
Writing - review & editing: Liang, H; Qiu, B; Liu, Z.
Funding acquisition, project administration, supervision and validation: Qiu, B; Liu, Z.

### Availability of data and materials

Some results supporting this study are presented in the Supplementary Materials. Other raw data that support the findings of this study are available from the corresponding author upon reasonable request.

### AI and AI-assisted tools statement

During the preparation of this manuscript, the AI tool ChatGPT (version 5.4, released 2026-3-5) was used solely for language editing. The tool did not influence the study design, data collection, analysis, interpretation, or the scientific content of the work. All authors take full responsibility for the accuracy, integrity, and final content of the manuscript.

### Financial support and sponsorship

This work was financially supported by the National Natural Science Foundation of China (Grant Nos. 52272253 and 52472266), the External Cooperation Program of the Chinese Academy of Sciences (Grant No. 181GJHZ2024126MI), the R&D Project of Jiangsu Province (Grant No. BG2024021), the "Innovation Yongjiang 2035" Key R&D Program (Grant No. 2025Z063), and the Natural Science Foundation of Ningbo (Grant No. 2024QL041).

### Conflicts of interest

All authors declared that there are no conflicts of interest.

### Ethical approval and consent to participate

Not applicable.

### Consent for publication

Not applicable.

## Copyright



## Supplementary Materials

Supplementary Materials

## REFERENCES


1. Manthiram, A. A reflection on lithium-ion battery cathode chemistry. *Nat. Commun.* **2020**, *11*, 1550. DOI PubMed PMC
2. Chen, H.; Xia, X.; Ma, J. Comprehensive review of Li-rich Mn-based layered oxide cathode materials for lithium-ion batteries: theories, challenges, strategies and perspectives. *ChemSusChem* **2024**, *17*, e202401120. DOI
3. Sathiya, M.; Rousse, G.; Ramesha, K.; et al. Reversible anionic redox chemistry in high-capacity layered-oxide electrodes. *Nat. Mater.* **2013**, *12*, 827-35. DOI
4. Seo, D. H.; Lee, J.; Urban, A.; Malik, R.; Kang, S.; Ceder, G. The structural and chemical origin of the oxygen redox activity in layered and cation-disordered Li-excess cathode materials. *Nat. Chem.* **2016**, *8*, 692-7. DOI PubMed
5. Assat, G.; Tarascon, J. Fundamental understanding and practical challenges of anionic redox activity in Li-ion batteries. *Nat. Energy.* **2018**, *3*, 373-86. DOI
6. Qiu, B.; Zhou, Y.; Liang, H.; et al. Negative thermal expansion and oxygen-redox electrochemistry. *Nature* **2025**, *640*, 941-6. DOI
7. Li, Q.; Ning, D.; Wong, D.; et al. Improving the oxygen redox reversibility of Li-rich battery cathode materials via coulombic repulsive interactions strategy. *Nat. Commun.* **2022**, *13*, 1123. DOI PubMed PMC
8. Gent, W. E.; Lim, K.; Liang, Y.; et al. Coupling between oxygen redox and cation migration explains unusual electrochemistry in lithium-rich layered oxides. *Nat. Commun.* **2017**, *8*, 2091. DOI PubMed PMC
9. Zhang, J.; Wang, Q.; Li, S.; et al. Depth-dependent valence stratification driven by oxygen redox in lithium-rich layered oxide. *Nat. Commun.* **2020**, *11*, 6342. DOI PubMed PMC
10. Marie, J. J.; House, R. A.; Rees, G. J.; et al. Trapped $O_2$ and the origin of voltage fade in layered Li-rich cathodes. *Nat. Mater.* **2024**, *23*, 818-25. DOI PubMed PMC
11. Ren, M.; Jiao, S.; Zhao, Y.; et al. Thermal decomposition mechanisms and inherent stability differences between $O_2$- and $O_3$-lithium-rich manganese-based oxide cathodes. *Adv. Funct. Mater.* **2026**, *36*, e30009. DOI
12. Lei, Y.; Ni, J.; Hu, Z.; et al. Surface modification of Li-rich Mn-based layered oxide cathodes: challenges, materials, methods, and characterization. *Adv. Energy. Mater.* **2020**, *10*, 2002506. DOI
13. Kou, P.; Zhang, L.; Zhang, Z.; et al. Oxygen vacancy engineering for high-performance Li-rich manganese cathodes: advances and prospects. *Energy. Storage. Mater.* **2025**, *79*, 104321. DOI
14. Qiu, B.; Zhang, M.; Wu, L.; et al. Gas-solid interfacial modification of oxygen activity in layered oxide cathodes for lithium-ion batteries. *Nat. Commun.* **2016**, *7*, 12108. DOI PubMed PMC
15. Zhao, J.; Su, Y.; Dong, J.; et al. Regulating anionic redox reversibility in Li-rich layered cathodes via diffusion-induced entropy-assisted surface engineering. *Energy. Storage. Mater.* **2024**, *70*, 103550. DOI
16. Luo, D.; Xie, H.; Tan, F.; et al. Scalable nitrate treatment for constructing integrated surface structures to mitigate capacity fading and voltage decay of Li-rich layered oxides. *Angew. Chem. Int. Ed. Engl.* **2022**, *61*, e202203698. DOI
17. Wang, F.; Zuo, P.; Xue, Z.; Liu, Y.; Wang, C.; Chen, G. Fluorination effect on lithium- and manganese-rich layered oxide cathodes. *ACS. Energy. Lett.* **2024**, *9*, 1249-60. DOI PubMed PMC
18. Jang, H. Y.; Eum, D.; Cho, J.; et al. Structurally robust lithium-rich layered oxides for high-energy and long-lasting cathodes. *Nat. Commun.* **2024**, *15*, 1288. DOI PubMed PMC
19. Li, B.; Zhuo, Z.; Zhang, L.; et al. Decoupling the roles of Ni and Co in anionic redox activity of Li-rich NMC cathodes. *Nat. Mater.* **2023**, *22*, 1370-9. DOI
20. Ravel, B.; Newville, M. Athena, Artemis, Hephaestus: data analysis for X-ray absorption spectroscopy using IFEFFIT. *J. Synchrotron. Radiat.* **2005**, *12*, 537-41. DOI PubMed
21. Bhamidi, V.; Kenis, P. J. A.; Zukoski, C. F. Probability of nucleation in a metastable zone: induction supersaturation and implications. *Crystal. Growth. Design.* **2017**, *17*, 1132-45. DOI
22. Liu, X. Y. Generic mechanism of heterogeneous nucleation and molecular interfacial effects. In: Advances in crystal growth research. Elsevier; 2001. pp 42-61. DOI
23. Lamer, V. K.; Dinegar, R. H. Theory, production and mechanism of formation of monodispersed hydrosols. *J. Am. Chem. Soc.* **1950**, *72*, 4847-54. DOI

24. Liu, X. Y. A new kinetic model for three-dimensional heterogeneous nucleation. *J. Chem. Phys.* **1999**, *111*, 1628-35. DOI
25. Fletcher, N. H. Size effect in heterogeneous nucleation. *J. Chem. Phys.* **1958**, *29*, 572-6. DOI
26. Yu, H.; So, Y. G.; Kuwabara, A.; et al. Crystalline grain interior configuration affects lithium migration kinetics in Li-rich layered oxide. *Nano. Lett.* **2016**, *16*, 2907-15. DOI
27. Yin, C.; Wei, Z.; Zhang, M.; et al. Structural insights into composition design of Li-rich layered cathode materials for high-energy rechargeable battery. *Mater. Today.* **2021**, *51*, 15-26. DOI
28. Kang, K.; Ceder, G. Factors that affect Li mobility in layered lithium transition metal oxides. *Phys. Rev. B.* **2006**, 74. DOI
29. Lanz, P.; Villevieille, C.; Novák, P. *Ex situ* and *in situ* Raman microscopic investigation of the differences between stoichiometric $LiMO_2$ and high-energy $xLi_2MnO_3\cdot(1\text{-}x)LiMO_2$ (M = Ni, Co, Mn). *Electrochimica. Acta.* **2014**, *130*, 206-12. DOI
30. Zhu, Z.; Yu, D.; Yang, Y.; et al. Gradient Li-rich oxide cathode particles immunized against oxygen release by a molten salt treatment. *Nat. Energy.* **2019**, *4*, 1049-58. DOI
31. Julien, C.; Massot, M. Lattice vibrations of materials for lithium rechargeable batteries I. Lithium manganese oxide spinel. *Mat. Sci. Eng. B-Adv.* **2003**, *97*, 217-30. DOI
32. Wu, T.; Liu, X.; Zhang, X.; et al. Full concentration gradient-tailored Li-rich layered oxides for high-energy lithium-ion batteries. *Adv. Mater.* **2021**, *33*, e2001358. DOI
33. Jarvis, K.; Wang, C.; Varela, M.; Unocic, R. R.; Manthiram, A.; Ferreira, P. J. Surface reconstruction in Li-Rich layered oxides of Li-ion batteries. *Chem. Mater.* **2017**, *29*, 7668-74. DOI
34. Hausbrand, R.; Cherkashinin, G.; Ehrenberg, H.; et al. Fundamental degradation mechanisms of layered oxide Li-ion battery cathode materials: methodology, insights and novel approaches. *Mat. Sci. Eng. B-Adv.* **2015**, *192*, 3-25. DOI
35. Zheng, J.; Xu, P.; Gu, M.; et al. Structural and chemical evolution of Li- and Mn-rich layered cathode material. *Chem. Mater.* **2015**, *27*, 1381-90. DOI
36. Bak, S.; Nam, K.; Chang, W.; et al. Correlating structural changes and gas evolution during the thermal decomposition of charged $Li_xNi_{0.8}Co_{0.15}Al_{0.05}O_2$ cathode materials. *Chem. Mater.* **2013**, *25*, 337-51. DOI
37. Wang, L.; Maxisch, T.; Ceder, G. A first-principles approach to studying the thermal stability of oxide cathode materials. *Chem. Mater.* **2007**, *19*, 543-52. DOI
38. Armstrong, A. R.; Holzapfel, M.; Novák, P.; et al. Demonstrating oxygen loss and associated structural reorganization in the lithium battery cathode $Li[Ni_{0.2}Li_{0.2}Mn_{0.6}]O_2$. *J. Am. Chem. Soc.* **2006**, *128*, 8694-8. DOI
39. Zhou, Y.; Cui, H.; Qiu, B.; et al. Sufficient oxygen redox activation against voltage decay in Li-rich layered oxide cathode materials. *ACS. Mater. Lett.* **2021**, *3*, 433-41. DOI
40. Kuball, M.; Hayes, J. M.; Suski, T.; et al. High-pressure high-temperature annealing of ion-implanted GaN films monitored by visible and ultraviolet micro-Raman scattering. *J. Appl. Phys.* **2000**, *87*, 2736-41. DOI
41. Baddour-Hadjean, R.; Pereira-Ramos, J. P. Raman microspectrometry applied to the study of electrode materials for lithium batteries. *Chem. Rev.* **2010**, *110*, 1278-319. DOI
42. Flores, E.; Novák, P.; Berg, E. J. *In situ* and *operando* Raman spectroscopy of layered transition metal oxides for Li-ion battery cathodes. *Front. Energy. Res.* **2018**, *6*, 82. DOI
43. Yu, X.; Lyu, Y.; Gu, L.; et al. Understanding the rate capability of high-energy-density Li-rich layered $Li_{1.2}Ni_{0.15}Co_{0.1}Mn_{0.55}O_2$ cathode materials. *Adv. Energy. Mater.* **2014**, *4*, 1300950. DOI
44. Myeong, S.; Cho, W.; Jin, W.; et al. Understanding voltage decay in lithium-excess layered cathode materials through oxygen-centred structural arrangement. *Nat. Commun.* **2018**, *9*, 3285. DOI PubMed PMC